Analyst

ROYAL SOCIETY OF CHEMISTRY

COMMUNICATION

View Article Online
View Journal | View Issue

Cite this: *Analyst*, 2021, **146**, 1163

Received 19th September 2020,
Accepted 22nd December 2020

DOI: 10.1039/d0an01880e

rsc.li/analyst

Visualizing intra-medulla lipids in human hair using ultra-multiplex CARS, SHG, and THG microscopy†

Daiki Kaneta,[a] Makiko Goto,[b] Motofumi Hagihara,[b] Philippe Leproux,[c,d] Vincent Couderc,[c] Mariko Egawa [b] and Hideaki Kano *[a,e]

We performed label-free imaging of human-hair medulla using multi-modal nonlinear optical microscopy. Intra-medulla lipids (IMLs) were clearly visualized by ultra-multiplex coherent anti-Stokes Raman scattering (CARS) spectroscopic imaging. Two groups of IMLs were found: second harmonic generation (SHG) active and inactive. By combining SHG analysis with CARS, the two groups were identified as free fatty acids and wax esters, respectively.

1. Introduction

Human hair has a three-layered structure. The cuticle, the outermost layer of hair, is chemically resistant, and protects the inner structure. The cortex, the major component of the hair mass, is composed of keratinized cortical cells and the cell-membrane complex. The medulla is the innermost structure and could be absent, fragmented or continuous.[1]

A number of analytical methods, including X-ray diffraction,[2,3] circular dichroism,[4,5] NMR spectroscopy,[6,7] and IR and Raman spectroscopies[8–10] have been used to determine the protein secondary structures in the cuticle and cortex of human hair. However, only a few chemical (spectroscopic or chromatographic) analyses of the medulla have been reported.[11–14] IR and Raman spectroscopies have provided strong evidence for the existence of intra-medulla lipids (IMLs). In particular, a C═O bond characteristic of an ester and a C–C bond (*trans*) have been detected by IR and Raman studies, respectively. However, the spatial resolution ever reported is not sufficient to localize and specify the IMLs clearly. Using chromatographic methods, the chemical composition of IMLs has been analyzed. Squalene and oleic acids have been detected,[15] but many other components remain unidentified. There is a need for additional analytical techniques.

Multimodal nonlinear optical microscopy has been widely used for investigating tissue and live-cell samples without labeling. In particular, multiplex CARS (M-CARS)[16] or broadband CARS (B-CARS)[17] microspectroscopy enables us to visualize molecular species in living cells and tissues with the use of the multiple vibrational resonances.[18–21]

Concerning the broadband multiplex CARS technique, Cheng *et al.*[16] and Wurpel *et al.*[22] reported the pioneering microscopic works on the development of M-CARS microscopy with the use of synchronized femtosecond and picosecond Ti:sapphire laser oscillators. Since they used two independent laser oscillators, sophisticated techniques were required to coincide the repetition rates of these two laser sources. Furthermore, the spectral coverage was limited to be ~300 cm^{-1} due to the spectral bandwidth of the femtosecond Stokes laser. The requirement of the synchronization was later overcome by using ultra-broadband supercontinuum (SC) light source.[23,24] Since the SC can be generated just by seeding a portion of the pump laser pulses into a tapered fiber[23] or photonic crystal fiber(PCF),[24] the pump and Stokes (SC) laser pulses are automatically synchronized. Moreover, owing to the ultra-broadband spectral coverage (>3000 cm^{-1}) of SC, it covers both the finger-print as well as the C–H, N–H, and O–H stretching region.[17,25] This technique is currently referred to as ultra-broadband multiplex CARS[24] (or ultra-multiplex CARS[21] as in the present study) or broadband CARS (B-CARS).[17–19]

In addition to CARS, multimodal nonlinear optical microscopy can detect other common nonlinear optical processes such as second harmonic generation (SHG), which can probe unique and non-centrosymmetric filamentous structures. For example, we previously found that ciliary rootlets composed of rootletin filaments[26] are SHG active, as is the

[a]*Department of Applied Physics, Graduate School of Pure and Applied Sciences, University of Tsukuba, 1-1-1 Tennodai, Tsukuba, Ibaraki 305-8573, Japan*
[b]*Shiseido Global Innovation Center, 1-2-11, Takashima, Nishi-ku, Yokohama, Kanagawa 220-0011, Japan*
[c]*Institut de Recherche XLIM, UMR CNRS No. 7252, 123 Avenue Albert Thomas, 87060 Limoges CEDEX, France*
[d]*LEUKOS, 37 Rue Henri Giffard, 87280 Limoges, France*
[e]*Department of Chemistry, Faculty of Science, Kyushu University, 744, Motooka, Nishi-ku, Fukuoka, Fukuoka 819-0395, Japan. E-mail: hkano@chem.kyushu-univ.jp*

†Electronic supplementary information (ESI) available. See DOI: 10.1039/d0an01880e

ventral nerve cord of the nematode *Caenorhabditis elegans*[27] Moreover, we found a photo-induced weak SHG signal in centrosymmetric polystyrene microspheres.[28] These findings indicate that our system can visualize hitherto unknown SHG-active organelles. In the present study, we use multimodal nonlinear optical imaging with the highly sensitive SHG channel to visualize the medulla of human hair.

2. Methods

2.1 Ultra-multiplex CARS spectroscopic imaging system

We used a home-built multi-modal nonlinear-optical-microscopy system. The details of the setup are described elsewhere.[27] Briefly, the main laser source was a custom-made, dual-fiber-output, synchronized laser source (OPERA HP, Leukos, Limoges, France). The first laser output, having a wavelength 1064 nm, temporal duration 50 ps, and repetition rate 1 MHz, was used as the pump beam (ω_1) for the CARS process. The second laser output delivered ultra-broadband supercontinuum (SC) radiation, which was obtained by wavelength conversion from 1064 nm fundamental radiation using a PCF. The near-infrared spectral components of SC could be used as the Stokes beam (ω_2). In our previous setup,[20] the pump beam was free-space propagating, while the Stokes beam originated from the PCF output. In order that the pump and Stokes pulses be temporally overlapped, a free-space, >5 m-long delay line had to be used on the pump path. On the contrary, here dual-fiber-output scheme significantly simplifies the experimental setup since the synchronisation between the pump and Stokes pulses can be adjusted by equalizing the fiber lengths of both arms, without the need for a delay line. Just after the pump and Stokes fiber outputs, the two beams were superimposed by a notch filter, and guided into a modified inverted microscope (ECLIPSE Ti, Nikon Corp., Tokyo, Japan). The sample was placed on a piezoelectric stage (Nano-LP200, Mad City Labs Inc., Madison, WI, USA) for three-dimensional(*xyz*) position selection. The full scanning range of the *xyz*-piezo stage was 200 μm.[3] The laser beams were tightly focused using a microscope objective (CFI Plan Apo 60× NA 1.27, water-immersion, Nikon Corp., Tokyo, Japan). The third-harmonic generation (THG) ($3\omega_1$), SHG ($2\omega_1$), and ultra-multiplex CARS ($2\omega_1$–ω_2) signals were collected using a second objective lens (Plan S Fluor 40× NA 0.6, Nikon Corp., Tokyo, Japan). The THG and SHG signals were detected using a spectrometer (SpectraPro300i; Princeton Instruments Inc., Trenton, NJ, USA) equipped with a CCD camera (PIXIS 100B; Princeton Instruments); the CARS signals were detected using a spectrometer (LS785; Princeton Instruments) equipped with a CCD camera (BLAZE 100HR; Princeton Instruments). The spectral coverage and spectral resolution of the CARS signal were ~3500 cm^{-1} and 8 cm^{-1}, respectively. The exposure time at each spatial position was 100 ms for SHG/THG and 50 ms for CARS. The overall exposure time of 100 ms was limited by detection of the weak SHG signal. On the other hand, the exposure time for the CARS signal was shorten to be 50 ms in order to avoid saturation of the CARS signal. It should be noted that even with the 50 ms exposure time, the CARS signal at the CH stretching vibrational mode was saturated at some areas of the field of view. The typical laser power was about 100 and 25 mW for the pump and the Stokes beams, respectively. The image size (pixels and microns) and step size are 61 × 61 pixels, 120 × 120 μm^2 and 0.5 μm, respectively.

2.2 Spontaneous Raman spectroscopy

We used a home-built Raman-microscopy system. A diode-pumped solid-state (DPSS) laser source (J200GS-11, KYOCERA SOC Corporation, Kanagawa, Japan) was used for the Raman excitation. The laser beam was introduced into a microscope objective (100× NA 1.3, Nikon Corp., Tokyo, Japan), and then a back scattered Raman signal was collected with the same objective. The Raman signal was guided into a polychromator (Omni-Λ, Zolix, Beijing, China) and finally detected by a CCD camera (PIXIS 100BR, Princeton Instruments).

2.3 Sample preparation

Human white hair without any chemical treatment history such as coloring or permanent waving was obtained from a 41-year-old asian female. White hair was used because the high melanin-granule content in pigmented hair induces sample destruction upon laser irradiation. Hairs were refrigerated without any chemical treatment until measurement, immersed in phosphate buffer solution (PBS), cut into small pieces, mounted on a slide glass, sandwiched with another coverslip, and sealed with enamel. The hair sample in the preparation was immersed in PBS.

Palmitic acid (FUJIFILM Wako), tripalmitin (Wako), and wax esters (bees wax) (Nacalai tesque) were purchased, and were used without further purification.

2.4 Data analysis

The spectral profile of the raw CARS signal was distorted due to the interference of the vibrationally resonant CARS signal with the so-called nonresonant background (NRB). In order to retrieve the imaginary part of the third-order nonlinear optical susceptibility,$\chi^{(3)}$, from the raw CARS signal, we used maximum entropy method(MEM).[29] The program code for MEM is essentially the same as the reported work in the reference.[29] For the MEM calculation, we used Igor Pro 6.22 (Wavemetrics, Portland, OR, USA). As shown in Fig. S1,† we confirmed that the Im[$\chi^{(3)}$] spectrum retrieved from the raw CARS spectrum of wax esters reproduced well the spontaneous Raman spectrum.

3. Results and discussion

Fig. 1(a) and (b) show an optical image of an intact hair and the corresponding CARS image. The CARS image was mapped out simply by using the raw CARS signal intensity at 1650 cm^{-1}, where the apparent peak was observed as shown in Fig. 1(c) (vertical solid line). The spectral profiles in red and

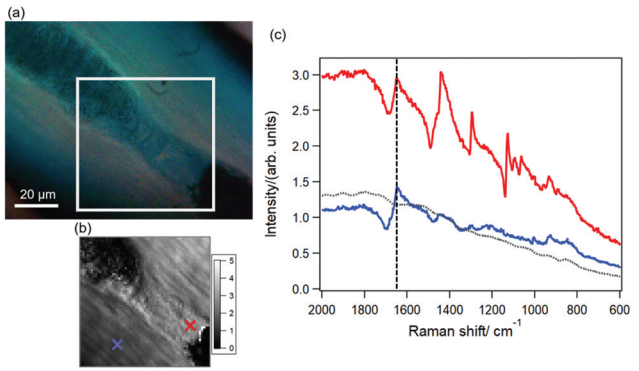

Fig. 1 (a) Optical image of an intact hair sample, (b) CARS intensity mapping at 1650 cm^{-1}. The image area corresponds to the white box indicated in (a), (c) spectral profiles of the raw CARS signal (red and blue) at red and blue crosses indicated in (b), corresponding to medulla and cortex. The vertical line represents the CARS signal at 1650 cm^{-1}, which was used in (b). The dotted curve (black) represents the CARS signal of the glass cover-slip underneath of the sample, which was assumed as non-resonant background (NRB).

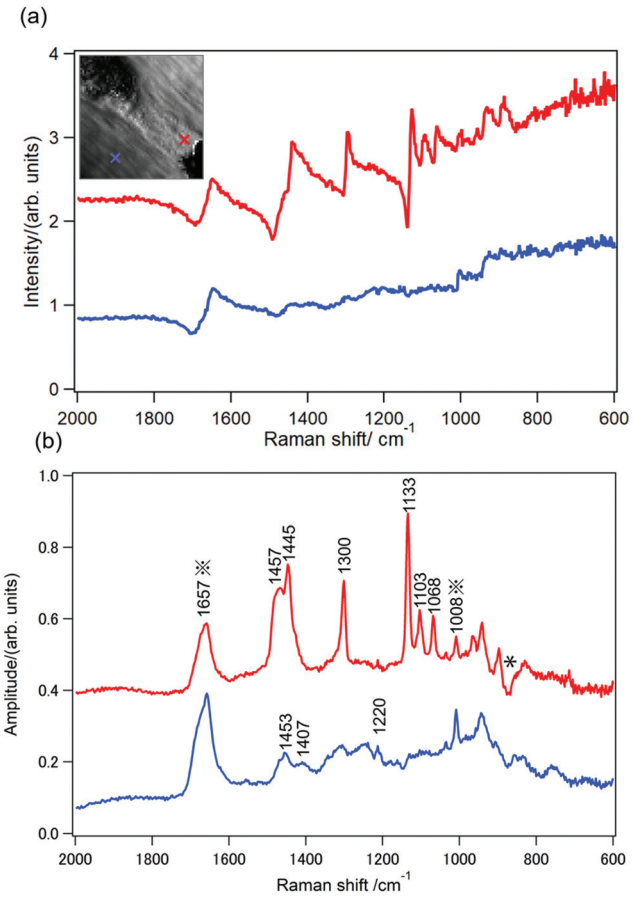

Fig. 2 (a) Intensity-corrected CARS spectra at the two positions indicated as red and blue crosses in Fig. 1(b) (also shown in the inset). The intensity-corrected CARS spectra were obtained by dividing the raw CARS spectra with the NRB obtained at the glass cover-slip (dotted curve in Fig. 1(c)). (b) Spontaneous-Raman-equivalent Im[$\chi^{(3)}$] spectra at the two positions indicated as red and blue crosses in the inset of Fig. 2(a), which were retrieved from the spectra in Fig. 2(a). The dip indicated by "*" is an artifact due to the weak vibrational resonance of a glass cover-slip.

blue in Fig. 1(c) were obtained at the positions of medulla (red cross in Fig. 1(b)) and of cortex (blue cross), respectively. The dotted line (black) in Fig. 1(c) represents the CARS signal of the glass cover-slip underneath of the sample, which was assumed as NRB, and was used for intensity correction of the CARS signal. As mentioned in 2.1, the exposure time of the CCD camera for the CARS signal was set to be 50 ms, which results in saturation of the CARS signal at the CH stretching region at some areas of the field of view. The ultra-multiplex CARS spectral profile without saturation was shown in Fig. S2† at the position of cortex different from the blue cross in Fig. 1(b).

As is well known, the band around 1650 cm^{-1} corresponds to amide I and/or *cis* C=C stretching vibrational modes, which are assigned as proteins and/or lipids, respectively. The raw CARS signal consists of both a vibrationally resonant signal and NRB; these interfere with each other and produce dispersive line shapes (see Fig. 1(c)). In order to extract the pure vibrationally resonant signal to obtain spontaneous-Raman-equivalent spectra, we performed the following procedures. First, the raw CARS spectral profiles were divided with that of NRB. The resultant intensity-corrected CARS spectra were shown in Fig. 2(a) at the same spatial positions as in Fig. 1. We then retrieved the pure vibrationally resonant spectra, which corresponds to the imaginary part of $\chi^{(3)}$ (Im[$\chi^{(3)}$]) spectra, from the spectra shown in Fig. 2(a) using MEM.[21] The Im[$\chi^{(3)}$] spectra are shown in Fig. 2(b).

The characteristic Raman bands are indicated in Fig. 2(b). The bands at 1657, 1457, 1445, 1300, 1133, 1068, 1008, and 895 cm^{-1} correspond to the vibrational modes due to amide I and/or *cis* C=C stretching, CH_3 degenerate deformation, CH_2 scissoring, CH_2 twisting, C–C(*trans*) stretching, C–C(*trans*) stretching, phenyl-ring breathing, and C_1–C_2(*trans*) stretching vibrational modes, respectively. The assignment of the sharp band observed at 1103 cm^{-1} is unclear, but is probably assignable as C–C stretching due to lipids. Since the CARS signal of the glass cover-slip, which we assumed as NRB, has weak vibrational resonance around 850 cm^{-1}, the broad spectral dip around 850 cm^{-1} in Fig. 2(b) is the artifact due to the vibrational resonance of the glass cover-slip.

We then analyzed the spectral profile of the Im[$\chi^{(3)}$] signal in more detail. Each band of Im[$\chi^{(3)}$] signal was first fitted using a Gaussian function or the sum of two Gaussian functions. Then, the amplitude of each band was mapped out. As a typical case, the result on the phenyl-ring breathing mode at 1008 cm^{-1}, which was fitted by a Gaussian function, was shown in Fig. S3(a).† Concerning the CH bending mode around 1450 cm^{-1}, the spectral profiles were complicated, and were clearly different between the protein-rich and lipid-rich areas. Therefore, we first fitted representative protein-rich and lipid-rich spectral profiles using the sum of two Gaussian func-

tions, and defined $f(\tilde{\nu})$ and $g(\tilde{\nu})$ as the protein-rich and lipid-rich representative spectral profiles, respectively. Here $\tilde{\nu}$ corresponds to Raman shift. Then, we fitted spectral profiles in all spatial points using the sum of $f(\tilde{\nu})$ and $g(\tilde{\nu})$ with two coefficients, namely $c_f f(\tilde{\nu}) + c_g g(\tilde{\nu})$. The representative protein-rich and lipid-rich spectral profiles ($f(\tilde{\nu})$ and $g(\tilde{\nu})$) as well as the decomposed each Gaussian function are indicated in Fig. S3(b) and (c).† Fig. 3 summarizes the results for main 9 vibrational modes.

As shown in Fig. 3, the microscopic structures of the hair were clearly visualized. The position of the medulla corresponds to the area around the white broken line with dark contrast in the optical image (Fig. 3(a)). The medulla and cortex are in the field of view, whereas the cuticle is not. Taking account of the CARS image contrast and literature data,[30–38] the bands shown in Fig. 3(b), (d), (f), (g), and (i) are assigned as follows: (b) C═O stretching (ester); (d) mainly CH_3 degenerate deformation (proteins); (f) mainly CH_2 twisting (lipids); (g) and (i) skeletal C–C(*trans*) stretching. These results are consistent with the previous reports.[11,12]

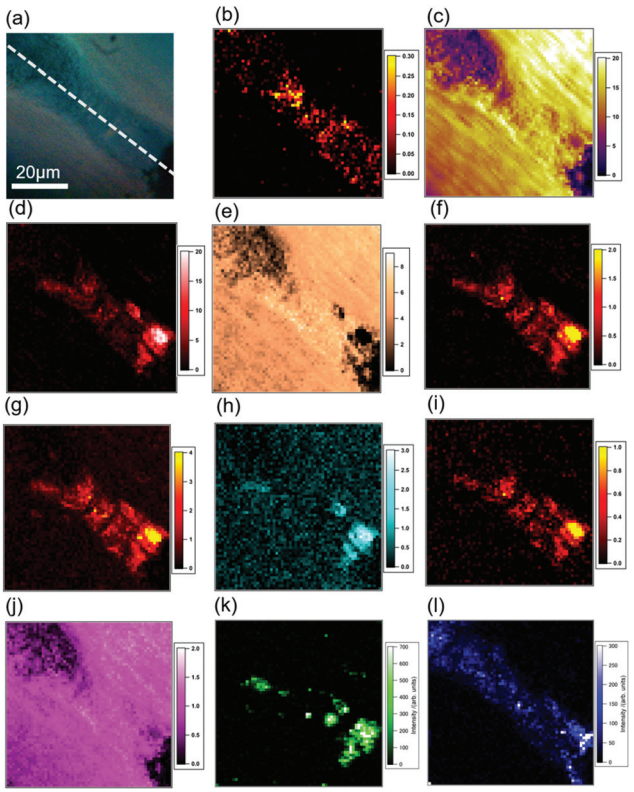

Fig. 3 (a) Optical image; CARS images of a hair sample at (b) C═O stretching (1741 cm^{-1}), (c) amide I (1665 cm^{-1}), (d) mainly CH_2 scissoring (lipids), (e) mainly CH_3 degenerate deformation (proteins), (f) CH_2 twisting (1300 cm^{-1}), (g) skeletal C–C(*trans*) (1134 cm^{-1}), (h) C–C stretching (1103 cm^{-1}), (i) skeletal C–C(*trans*) (1067 cm^{-1}), and (j) phenyl ring breathing (1008 cm^{-1}); (k) SHG, (l) THG. The spectral profile was fitted by a Gaussian function for (b), (c), (f), (g), (h), (i), (j), (k), and (l). The spectral profile of the CH bending vibrational mode ((d) and (e)) was fitted by the sum of the representative protein-rich (Fig. S3(b)†) and lipid-rich (Fig. S3(c)†) spectral profiles, as described in the main text.

The CARS images in Fig. 3(c), (e), and (j) illustrate the fibrous structure of the cortex. These images mainly visualize keratin protein, which is abundant in the cortex. They are ascribed to (c) amide I and/or *cis* C═C stretching, (e) mainly CH_3 degenerate deformation, and (f) phenyl-ring breathing vibrational modes, respectively. On the other hand, Fig. 3(k) and (l) also show bright areas in medulla.

In the present study, we unexpectedly found an SHG signal in the medulla. In order to identify SHG-active molecular species, we performed a combined analysis using SHG and CARS. Fig. 4 summarizes the results. Fig. 4(a), (b), (c) and (d) are the SHG image, the CARS images due to CH_2 twisting and C═O stretching vibrational modes, and the spectral profile of the Im[$\chi^{(3)}$] signal, respectively. The spectral profile (orange in Fig. 4(d)) from the SHG-active area A (orange circle in Fig. 4(a–c)) is similar to that of typical of fatty acids (FAs), such

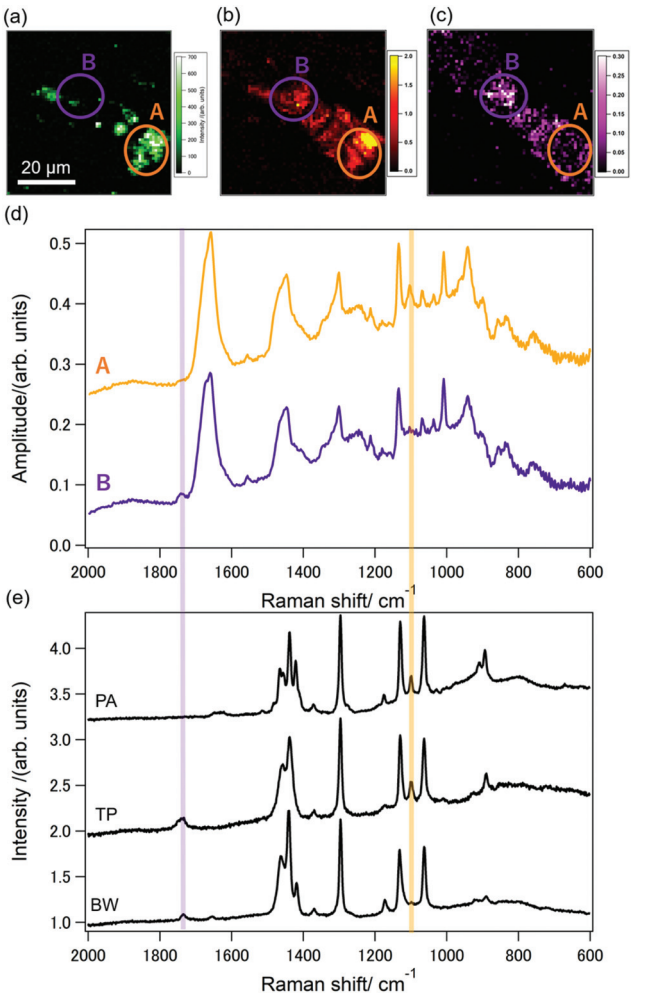

Fig. 4 (a) CARS image of human hair at 1300 cm^{-1} (CH_2 twisting), (b) SHG Image, (c) CARS image at 1741 cm^{-1} (C═O stretching), (d) spectral profiles of Im[$\chi^{(3)}$] signal at the two areas, A and B in (a), (e) Spontaneous Raman spectra of palmitic acid (PA), tripalmitin (TP), and bees wax (BW). Characteristic marker bands are indicated by the bright orange (fatty acids) and purple (esters) bars in (d) and (e).

as palmitic acid (PA) in Fig. 4(e). A characteristic marker band is indicated by the bright orange bar in Fig. 4(d) and (e). The sharp bands at 1130 cm^{-1} and 1063 cm^{-1}, assigned to C–C (*trans*), are marker bands of solid-phase lipids, which are observed in three spectra in Fig. 4(e). According to the literature,[13] FAs are one of the main lipids in hair. Thus, the SHG-active area in the medulla corresponds to solid FAs.

We found that another lipid-rich area in the medulla, indicated by the purple circle (B) in the images, is SHG inactive. In order to elucidate the difference between areas *A* and *B*, we performed an $Im[\chi^{(3)}]$ spectral analysis. The spectral profile (purple in Fig. 4(d)) of the $Im[\chi^{(3)}]$ signal from the SHG-inactive area shows a band at 1750 cm^{-1}, which is assigned as C═O due to ester. By comparing the spectrum with the spectral profiles of a triacylglycerol (tripalmitin; TP) and a wax esters(WEs) (bee wax; BW) (Fig. 4(e)) and the literature data,[13] we identified the lipid-rich and SHG-inactive molecular species as WEs. Although the mechanism of difference of SHG activity between FAs and WEs is not clear, SHG activity was confirmed by *in vitro* experiment. No SHG signal was observed in solid-phase BW, while SHG signal was observed in solid-phase PA.

Conclusions

In conclusion, we successfully visualized two different kinds of IMLs of human-hair medulla. By combining CARS and SHG analysis, we identified the two kinds, which are SHG-active and inactive, respectively, as FAs and WEs. It should be emphasized that the conventional spontaneous Raman microscopy cannot elucidate the SHG activity of intra-medulla lipids, because the laser source is typically continuous wave, which does not have enough peak power to generate the SHG signal. Our technique can be applied to elucidating other unknown molecular species in tissue samples.

Author contributions

D. K. primarily performed experimental work on CARS, SHG, and THG including the data analysis. M. G. and M. H. conceived validations of hair analysis, prepared the samples. P. L. and V. C. developed the laser source. M. E. conceived validations of hair analysis. H. K. conceived techniques of construction of multi-modal nonlinear optical microscope, analyzed the data. D. K., M. E., and H. K. wrote the manuscript with contributions from all authors.

Conflicts of interest

There are no conflicts to declare.

Acknowledgements

The authors gratefully acknowledge the assistance of J. Ukon of Ukon Craft Science, Ltd, for establishing a fruitful collaboration between Japanese and French laboratories. This study was financially supported by JSPS KAKENHI Grant Number 18H02000 (Grant-in-Aid for Scientific Research [B]).

References

1 D. W. Deedrick and S. L. Koch, *Forsensic Sci. Commun.*, 2004, **6**(1), 1–22.
2 R. S. Bear, *J. Am. Chem. Soc.*, 1944, **66**, 1297–1305.
3 R. S. Bear, *J. Am. Chem. Soc.*, 1944, **66**, 2043–2050.
4 N. J. Greenfield, *Nat. Protoc.*, 2007, **1**, 2876–2890.
5 L. Whitmore and B. A. Wallace, *Biopolymers*, 2008, **89**, 392–400.
6 D. S. Wishart, B. D. Sykes and F. M. Richards, *Biochemistry*, 1992, **31**, 1647–1651.
7 D. S. Wishart and B. D. Sykes, *J. Biomol. NMR*, 1994, **4**, 171–180.
8 W. K. Surewicz, H. H. Mantsch and D. Chapman, *Biochemistry*, 1993, **12**, 44–44.
9 P. R. Carey, *Annu. Rev. Phys. Chem.*, 2006, **57**, 527–554.
10 M. N. Kinalwa, E. W. Blanch and A. J. Doig, *Anal. Chem.*, 2010, **82**, 6347–6349.
11 L. Kreplak, F. Briki, Y. Duvault, J. Doucet, C. Merigoux, F. Leroy, J. L. Lévêque, L. Miller, G. L. Carr, G. P. Williams and P. Dumas, *Int. J. Cosmet. Sci.*, 2001, **23**, 369–374.
12 G. Zhang, L. Senak and D. J. Moore, *J. Biomed. Opt.*, 2011, **16**, 056009–056009.
13 Y. Masukawa, H. Tsujimura and G. Imokawa, *J. Chromatogr.*, 2005, **823**, 131–142.
14 M. Zimmerley, J. Ward, J. Marsh, D. Oertel and E. O. Potma, *Biomedical Optics and 3-D Imaging, OSA Technical Digest*, 2010, BTuD77, DOI: 10.1364/biomed.2010.btud77.
15 J. Ymazaki and K. Maeda, *Cosmetics*, 2018, **5**, 1–12.
16 J.-X. Cheng, A. Volkmer, L. D. Book and X. S. Xie, *J. Phys. Chem. B*, 2002, **106**, 8493–8498.
17 S. H. Parekh, Y. J. Lee, K. A. Aamer and M. T. Cicerone, *Biophys. J.*, 2010, **99**, 2695–2704.
18 C. H. Camp Jr., Y. J. Lee, J. M. Heddleston, C. M. Hartshorn, A. R. Hight Walker, J. N. Rich, J. D. Lathia and M. T. Cicerone, *Nat. Photonics*, 2014, **8**, 627–634.
19 C. H. Camp Jr. and M. T. Cicerone, *Nat. Photonics*, 2015, **9**, 295.
20 H. Yoneyama, K. Sudo, P. Leproux, V. Couderc, A. Inoko and H. Kano, *APL Photonics*, 2018, **3**, 092408.
21 H. Kano, T. Maruyama, J. Kano, Y. Oka, D. Kaneta, T. Guerenne, P. Leproux, V. Couderc and M. Noguchi, *OSA Continuum*, 2019, **2**, 1693–1705.
22 G. W. H. Wurpel, J. M. Schins and M. Müller, *Opt. Lett.*, 2002, **27**, 1093–1095.

23 T. W. Kee and M. T. Cicerone, *Opt. Lett.*, 2004, **29**, 2701–2703.
24 H. Kano and H. Hamaguchi, *Appl. Phys. Lett.*, 2005, **86**(12), 121113, DOI: 10.1063/1.1883714.
25 M. Okuno, H. Kano, P. Leproux, V. Couderc and H. Hamaguchi, *Opt. Lett.*, 2008, **33**, 923–925.
26 T. Akiyama, A. Inoko, Y. Kaji, S. Yonemura, K. Kakiguchi, H. Segawa, K. Ishitsuka, M. Yoshida, O. Numata, P. Leproux, V. Couderc, T. Oshika and H. Kano, *Sci. Rep.*, 2017, **7**, 39967.
27 S. Miyazaki, P. Leproux, V. Couderc, Y. Hayashi and H. Kano, *Appl. Phys. Express*, 2020, **13**, 072002.
28 K. Makihara, D. Kaneta, T. Iwamura, A. Sugita, P. Leproux, V. Couderc and H. Kano, *Appl. Phys. Express*, 2020, **13**, 052003.
29 E. M. Vartiainen, H. A. Rinia, M. Müller and M. Bonn, *Opt. Express*, 2006, **14**, 3622–3630.
30 T. Shimanouchi, *J. Phys. Chem. Ref. Data*, 1977, **6**, 993–1102.
31 Q. Matthews, A. Brolo, J. Lum, X. Duan and A. Jirasek, *Phys. Med. Biol.*, 2011, **56**, 19–38.
32 M. T. Cicerone and C. H. Camp, *Analyst*, 2017, **143**, 33–59.
33 C. Krafft, L. Neudert, T. Simat and R. Salzer, *Spectrochim. Acta, Part A*, 2005, **61**, 1529–1535.
34 B. W. Barry, H. G. M. Edwards and A. C. Williams, *J. Raman Spectrosc.*, 1992, **23**, 641–645.
35 H. Deng, V. A. Bloomfield, J. M. Benevides and G. J. Thomas, *Biopolymers*, 1999, **50**, 656–666.
36 R. G. Snyder, H. L. Strauss and C. A. Elliger, *J. Phys. Chem.*, 1982, **86**, 5145–5150.
37 R. G. Snyder and J. R. Scherer, *J. Chem. Phys.*, 1979, **71**, 3221–3228.
38 K. G. Brown, E. Bicknell-Brown and M. Ladjadj, *J. Phys. Chem.*, 1987, **91**, 3436–3442.